Dalton Transactions

ARTICLE

3D Hetero-structured Cobalt Oxide@Layered Double Hydroxide Core-shell Networks on Nickel Foam for High-performance Hybrid Supercapacitor

Received 00th January 20xx,
Accepted 00th January 20xx

DOI: 10.1039/x0xx00000x

www.rsc.org/

Luojiang Zhang,[a,b] K.N. Hui,*[c] K.S. Hui,*[d] Siu Wing Or *[a,b]

High performance of an electrode relies largely on a scrupulous design of nanoarchitectures and smart hybridization of bespoke active materials. Here, a 3D hetero-structured core-shell architecture is fabricated as supercapacitor electrode, in which Co_3O_4 nanowire cores are grown on nickel foam prior to in situ deposition of layered double hydroxide (LDH) nanosheet shells. Due to the unique configuration and hybridization, the as-fabricated Co_3O_4@LDH core-shell electrode exhibits a high capacity of 818.6 C g^{-1} at 2 A g^{-1} and 479.3 C g^{-1} at 40 A g^{-1} (3.2 C cm^{-2} at 7.8 mA cm^{-2} and 1.87 C cm^{-2} at 156 mA cm^{-2}), which are much better than those of the individual component of Co_3O_4 and LDH. A hybrid supercapacitor using Co_3O_4@LDH as positive electrode and graphene nanosheets as negative electrode yields an energy density of 53.2 Wh kg^{-1} and a power density of 16.4 kW kg^{-1}, which outperform the reported devices in the literature; the device also shows a long-term cycling stability which retains 71% of its initial capacity even after 10000 cycles at 6 A g^{-1}. The rational design of core-shell architecture may develop new strategies for fabricating promising electrode materials for electrochemical energy storage.

Introduction

As an important complement to rechargeable batteries and electrolytic capacitors, supercapacitors (SCs) embed core competency for next-generation power devices due to the advantages of high power density, rapid charge-discharge rate and long lifetime.[1, 2] In the past decades, an enormous amount of research work has been devoted to pseudocapacitor in which transitional metal oxides/hydroxides [3] and conducting polymers [4] are served as electroactive materials because they can offer much higher capacitance than electrical double-layer capacitors (carbonous materials as the electrode materials).[5]

Among the varied pseudocapacitive materials, layered double hydroxide (LDH) has caused wide public concern because of their high redox activity and relatively low cost.[6-8] However, similar to other transition metal oxides/hydroxides, their electrochemical behaviour like high-rate performance and cycle life have been greatly restrained due to the intrinsic insulation and highly packed morphology.[9-11] Therefore, it is very crucial to design LDH-based electrode materials with rational architecture to increase the electroactive sites and charge transfer kinetics for high performance SCs.[12]

Recently, materials with hetero-structured core-shell architecture have been demonstrated to exhibit great benefits for high performance SCs due to the synergetic effect of each component.[13, 14] For instance, NiCo-LDH nanosheets[15, 16] loaded on the surface of carbon materials have been reported as electrodes for SCs. However, in these papers,[15, 16] the carbon nanotubes just served as the conductive supports to deposit LDH to get enhanced specific surface area and conductivity. Instead, the electrodes with pseudocapacitive species as substrates and core materials are of great interests.[17-19] They not only serve as an agent to load shell materials with improved surface area but also contribute to the total capacitance owing to their own high electrochemical activities. When compared with powdery electrode materials, practically, the in situ growth of pseudocapacitive species on nickel foam (NF) has been applied more widely as the substrates due to their relatively simple preparation of electrodes, nonuse of binders and so on. [20] Taking into the consideration of challenges and opportunities, creating integrated smart architectures with well-defined structures, improved electroactivity, and faster ion and electron transport is timely and important.

Herein, we reported a stepwise hydrothermal approach to fabricate 3D hierarchical Co_3O_4@LDH core-shell networks (NWs) directly grown on NF as a binder-free electrode for high-performance supercapacitor, where the 1D Co_3O_4 nanowire arrays (NWAs) growing on NF acting as the "core" and NiAl-LDH nanosheets (NSs) working as the "shell". Such unique

[a] Department of Electrical Engineering, The Hong Kong Polytechnic University, Hung Hom, Kowloon, Hong Kong. E-mail: eeswor@polyu.edu.hk
[b] Hong Kong Branch of National Rail Transit Electrification and Automation Engineering Technology Research Center, Hong Kong. E-mail: eeswor@polyu.edu.hk
[c] Institute of Applied Physics and Materials Engineering, University of Macau, Avenida da Universidade, Taipa, Macau. E-mail: bizhui@umac.mo
[d] School of Mathematics, University of East Anglia, Norwich, NR4 7TJ, United Kingdom. E-mail: k.hui@uea.ac.uk

architecture can offer much larger interfacial area and channels for rapid ions diffusion and fast electron transports, which endows the designed Co_3O_4@LDH electrode with an excellent capacitive performance. The as-prepared Co_3O_4@LDH electrode exhibited a specific capacity of 818.6 C g^{-1} at a current density of 2 A g^{-1} and 479.3 C g^{-1} at 40 A g^{-1}, which were better than those of the individual component of Co_3O_4 and LDH electrodes. In addition, a hybrid supercapacitor (HSC) with Co_3O_4@LDH as positive electrode and graphene nanosheets (GNS) as negative electrode demonstrated a high energy density of 53.2 Wh kg^{-1} and outstanding cycling stability (71% of its initial capacity after 10000 cycles at a current density of 6 A g^{-1}), which outperformed the reported devices in the literature.[21] The rational design of LDH based core-shell architecture may open up new strategies for fabricating promising electrode materials with good energy storage performance for electrochemical energy storage.

Experimental Section

Materials preparation

All chemicals were of analytical grade and used as received without any further treatment. Cobalt nitrate hexahydrate [$Co(NO_3)_2{\cdot}6H_2O$, 98%, Acros Organics], nickel nitrate hexahydrate [$Ni(NO_3)_2{\cdot}6H_2O$, 99%, Acros Organics], aluminium nitrate nonahydrate [$Al(NO_3)_3{\cdot}9H_2O$, 99%, Acros Organics], urea [$CO(NH_2)_2$, 99%, Acros Organics], ammonium fluoride [NH_4F, 98%, Acros Organics]. Nickel foam (110 PPI, 31 mg cm^{-2}) was purchased from Shenzhen Kejingstar Technology LTD. (China).

Synthesis of 1D Co_3O_4 NWAs on NF: NF was pre-treated with 6.0 M HCl, deionized water, and absolute ethanol, each for 20 min. 1.20 g of urea was dissolved into 50 mL 0.08 M $Co(NO_3)_2{\cdot}6H_2O$ to form a homogeneous pink solution. After that, a cleaned NF (10 × 10 × 1 mm) was dipped into the above solution and transferred into a 100-mL Teflon-lined stainless-steel autoclave which was sealed and maintained at 95 °C for 10 h, and then cooled down to ambient temperature naturally. Finally, the NF loaded product (precursor) was taken out, washed, vacuum dried and then thermally treated at 250 °C in air for 1 h to get crystallized Co_3O_4 NWAs. The mass of Co_3O_4 NWAs on NF was determined by subtracting the weight before deposition from the weight after calcination. Co_3O_4 NWAs loading was approximately 2.7 mg for all electrodes.

Synthesis of 3D Co_3O_4@LDH NWs on NF: 3D Co_3O_4@LDH hierarchical structures were prepared by growing NiAl-LDH NSs onto the Co_3O_4 NWAs backbones via a second hydrothermal process. Typically, the as-obtained NF-supported Co_3O_4 NWAs was immersed in a 100-mL Teflon autoclave with homogeneous solution of 0.291 g $Ni(NO_3)_2{\cdot}6H_2O$, 0.125 g $Al(NO_3)_3{\cdot}9H_2O$, 0.267 g urea, 0.099 g NH_4F and 70 mL of deionized water; the autoclave was then maintained at 120 °C for 5 h. Finally, the NF loaded sample was removed out, washed with deionized water and ethanol, and dried at 60 °C to obtain a hierarchical Co_3O_4@LDH core-shell NWs. Co_3O_4@LDH NWs loading was approximately 3.9 mg for all electrodes. For comparison, the bare NiAl-LDH NSs growth on NF (labeled as LDH NSs) was also obtained using a similar approach with the pure NF. LDH loading was approximately 0.9 mg for all electrodes.

Material characterizations

X-ray diffraction (XRD, Bruker D8 Advance X-ray) of the samples was performed using Cu Kα radiation (λ = 0.15406 nm) at 40 kV and 30 mA. The scanning speed was 5° min-1 with a 0.02° step. The morphology and structural properties of the samples were observed by scanning electron microscopy (SEM, LEO-1550) with an applied voltage of 5 kV and transmission electron microscope (TEM, JEM-2100F).

Electrochemical measurement

Electrochemical measurements were carried out in 6 M KOH electrolyte at room temperature on a ZIVE SP2 electrochemical working station instrument. Each electrode was first measured in a three-electrode system which composed of a working electrode, a platinum foil counter electrode and an Hg/HgO reference electrode. Co_3O_4 NWAs, Co_3O_4@LDH NWs or LDH NSs growing on NF were directly used as working electrodes, respectively. Cyclic voltammetry (CV) tests were performed between 0 and 0.65 V (vs. Hg/HgO) to avoid serious polarization at a scan rate of 5 mV s^{-1}. Galvanostatic charge-discharge (GCD) curves were measured in a potential window of 0 ~ 0.6 V (vs. Hg/HgO) due to the polarization at different current densities. Cycle stability measurements were tested at 20 A g^{-1} for 10000 cycles. A frequency from 100 kHz to 0.01 Hz at the open circuit potential with an AC perturbation of 5 mV was set in the electrochemical impedance spectroscopy (EIS) measurements.

An HSC was assembled using Co_3O_4@LDH NWs as the positive electrode and GNS as the negative electrode in a 6 M KOH electrolyte solution. The negative electrode for the HSC was prepared by mixing GNS (80 wt.%) with acetylene black (10 wt.%) and polytetrafluoroethylene (PTFE, 10 wt.%) in a few drops of water. The adding of acetylene black was to make up the loss conductivity caused by the introduction of insulating PTFE binder. After coating the slurry on a clean NF (10 × 10 × 1 mm), the electrodes were dried at 50 °C for 12 h before pressing under pressure of 20 MPa. CV and GCD measurements were performed both between 0 and 1.6 V at different scan rates and current densities, respectively.

Results and Discussion

Synthesis and characterizations

The crystallographic natures of NF loaded precursor, Co_3O_4 NWAs, Co_3O_4@LDH NWs and LDH NSs were verified by XRD, as depicted in **Fig. 1**. In all patterns, three strong peaks marked by "•" ($2\theta = 45^o$, 52^o and 76^o) belong to the NF substrate (JCPDS card no: 04-0850). For the precursor, except for the peaks arising from the NF, all of the other diffraction peaks are in good agreement with $Co(CO_3)_{0.5}(OH){\cdot}0.11H_2O$ (JCPDS card no: 48-0083) which is formed from the reaction of Co^{2+} and urea.[22] After heat treatment and LDH deposition, the diffraction peaks

appeared in Co_3O_4@LDH NWs are well indexed with those in cubic phase Co_3O_4 (JCPDS card no: 42-1467, marked by "◆") and hydrotalcite-like NiAl-LDH ($Ni_6Al_2(OH)_{16}(CO_3,OH)\cdot 4H_2O$, JCPDS card no: 15-0087, marked by "▽"), indicating that hetero-structured architecture has been successfully prepared.

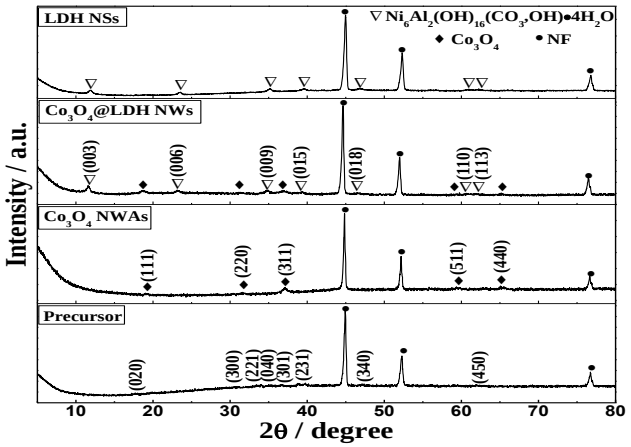

Fig. 1 XRD patterns of NF loaded precursor, Co_3O_4 NWAs, Co_3O_4@LDH NWs and LDH NSs.

The morphologies of NF loaded precursor, Co_3O_4 NWAs, Co_3O_4@LDH NWs and LDH NSs were investigated by SEM in **Fig. 2**. Fig. 2a shows the SEM image of the $Co(CO_3)_{0.5}(OH)$ precursor. It can be seen that large-scale, dense grass-like clusters grown uniformly on the skeletons of NF. A careful examination (Fig. 2b) reveals that these grass-like clusters are made up of multi-directional nanowires. After heat treatment, the grass-like clusters transform into 1D well-aligned Co_3O_4 NWAs (Fig. 2c) with an uneven surface texture, clearly exhibiting granular characteristics (Fig. 2d). The average diameter of the nanowire is determined to be about 50 nm and the length can be up to several micrometers. After the second hydrothermal growth, thin corrugated NiAl-LDH layers cover vertically on the entire surface of each Co_3O_4 nanowire to form a 3D core-shell network structure (Fig. 2e). Significantly, the morphology and alignment of Co_3O_4 nanowires are still well maintained even after the deposition of NiAl-LDH and each nanowire is separated apart adequately. From the high magnification SEM image (Fig. 2f), it can be found that the deposited NiAl-LDH nanosheets with thickness of several nanometers are interconnected with each other to form a highly porous configuration. The pores or voids between the nanowires and nanosheets of both the core and shell are beneficial to the electrolyte infiltration, allowing the fast ion and electron transportation.[23] Unlike the corrugated layer of NiAl-LDH in core-shell Co_3O_4@LDH NWs material, the bare LDH NSs, which aligned vertically on the surface of NF, possesses a nanostructure composed of flat nanosheets with an average thickness of 20 nm (Fig. 2g and 2h).

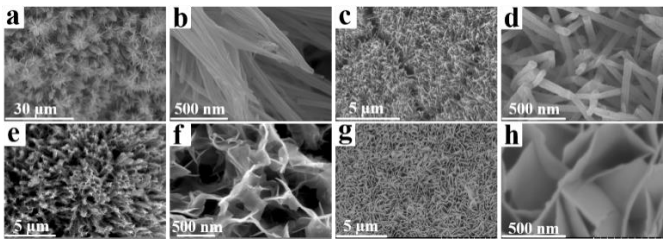

Fig. 2 SEM images of NF loaded precursor (a, b), Co_3O_4 NWAs (c, d), Co_3O_4@LDH NWs (e, f) and LDH NSs (g, h)

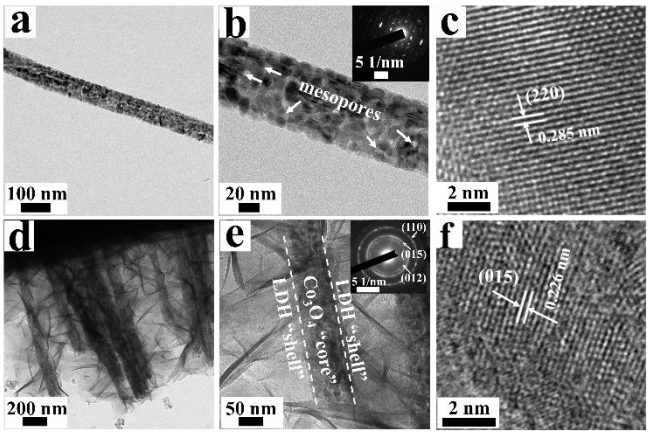

Fig. 3 TEM images (a, b) and HRTEM image (c) of Co_3O_4 NWAs. TEM images (d, e) and HRTEM image (f) of Co_3O_4@LDH NWs core-shell structure.

More detailed structural information was also discerned from TEM (**Fig. 3**), which demonstrated the 1D porous texture of Co_3O_4 NWAs and the 3D core-shell structure of Co_3O_4@LDH NWs. Fig. 3a and 3b exhibit the TEM images of Co_3O_4 NWA scraped off from NF substrate, from which it can be clearly found that the diameter of the single nanowire is around 50 nm, consistent with the SEM result (Fig. 2d). Moreover, the nanowire is consisted of numerous Co_3O_4 particles (Fig. 3b), leading to the formation of lots of mesopores which results from the release of H_2O and CO_2 gas during the heat treatment [24]. Meanwhile, the selected area electron diffraction (SAED) pattern (inset of Fig. 3b) demonstrates a polycrystalline structure of the Co_3O_4 nanowire. The lattice spacing of 0.285 nm is corresponded to the (220) crystal plane of Co_3O_4, as seen from the HRTEM image (Fig. 3c). Note that the porous and crystalline Co_3O_4 nanowires show a specific structure that could be used as a scaffold for nucleation and growth of NiAl-LDH nanosheets, which is favourable for electrochemical energy storage. Comparatively, Fig. 3d and 3e display that Co_3O_4@LDH NWs possess a peculiar core-shell structure in which thin NiAl-LDH nanosheets uniformly cover the surface of the porous Co_3O_4 nanowire. The diffraction rings of SAED pattern (inset of Fig. 3e) can be indexed to (012), (015) and (110) facets of NiAl-LDH which are consistent with the XRD result in Fig. 1. HRTEM (Fig. 3f) reveals that the nanosheet has a visible lattice fringe of 0.226 nm, corresponding well to the (015) plane of NiAl-LDH.

The proposed synthetic procedure of 3D Co_3O_4@LDH NWs core-shell architecture on the NF involves hydrothermal

precipitation, annealing and a second hydrothermal process, as schematically illustrated in **Fig. 4**. Initially, uniform pink $Co(CO_3)_{0.5}(OH)$ precursors were grown directly on NF substrate via a facile hydrothermal reaction of Co^{2+} and urea;[25] and further annealing of $Co(CO_3)_{0.5}(OH)$ precursors enabled the formation of black porous Co_3O_4 NWAs; after that, the obtained porous nanowires were designed as a scaffold for the following structural construction of NiAl-LDH shells through a second hydrothermal reaction. Finally, the Co_3O_4@LDH core-shell networks were obtained and the colour of the NF surface turned into deep brown. The relevant reactions are illustrated as follows (Equation 1-6):

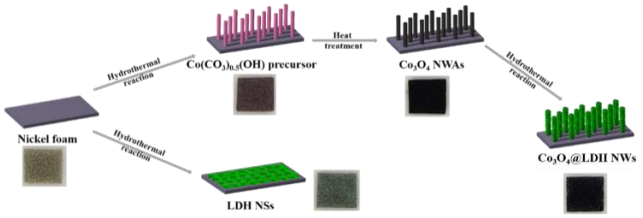

Fig. 4 Schematic illustration of the fabrication of 3D Co_3O_4@LDH NWs core-shell material.

$CO(NH_2)_2 + H_2O \rightarrow 2NH_3 + CO_2$ … (1)

$CO_2 + H_2O \rightarrow CO_3^{2-} + 2\,H^+$ … (2)

$NH_3 + H_2O \rightarrow NH_4^+ + OH^-$ … (3)

$Co^{2+} + 0.5CO_3^{2-} + OH^- + nH_2O \rightarrow Co(CO_3)_{0.5}(OH)\cdot nH_2O$ … (4)

$6Co(CO_3)_{0.5}(OH)\cdot nH_2O + 5O_2 \xrightarrow{\Delta} Co_3O_4 + 3(2n+1)H_2O\uparrow + 9CO_2\uparrow$ … (5)

$6Ni^{2+} + 2Al^{3+} + 0.5CO_3^{2-} + 17OH^- + 4H_2O \rightarrow Ni_6Al_2(OH)_{16}(CO_3, OH)\cdot 4H_2O$ … (6)

The Co_3O_4 NWAs consist of numerous interconnected nanoparticles with a large quantity of mesoporous structures, which is ascribed to the successive release and loss of CO_2 and H_2O during the thermal decomposition of $Co(CO_3)_{0.5}(OH)\cdot nH_2O$ precursor.[26] In contrast, bare LDH NSs were also directly deposited on NF with the colour turned to light green.

Electrochemical measurements

To investigate the electrochemical properties of the obtained electrodes, CV, GCD and EIS measurements were conducted first in a three-electrode system. **Fig. 5**a shows the CV curves of NF loaded Co_3O_4 NWAs, LDH NSs and Co_3O_4@LDH NWs at a scan rate of 5 mV s^{-1}. Redox peaks could be clearly observed for each curve, which is a typical characteristic of Faradaic behaviour of these electrodes.[27] For Co_3O_4 NWAs, the peaks are ascribed to the Faradaic redox process of Co_3O_4/CoOOH and CoOOH/CoO_2, which are described as follows (Equation 7 and 8):[28]

$Co_3O_4 + OH^- + H_2O \leftrightarrow 3CoOOH + e^-$ … (7)

$CoOOH + OH^- \leftrightarrow CoO_2 + H_2O + e^-$ … (8)

For LDH NSs, the redox peaks are attributed to the conversion of Ni^{2+} to Ni^{3+} based on the following reaction (Equation 9):[9, 27]

$Ni(OH)_2 + OH^- \leftrightarrow NiOOH + H_2O + e^-$ … (9)

In contrast, the CV curve of Co_3O_4@LDH NWs electrode shows the largest integral area, indicating a higher specific capacity and electrochemical activity than the individual components. A comparison of the GCD profiles at a current density of 2 A g^{-1} plotted in Fig. 5b further demonstrates this finding. Areal (C_a) and gravimetric specific capacity (C_g) can be calculated from the discharge curves following the Equation (10) and (11), respectively:

$C_a = I \times \Delta t / S$ … (10)

$C_g = I \times \Delta t / m$ … (11)

where I is the discharge current (A), Δt is the discharge time (s), S is the geometrical area of the electrode (cm^2), m is the mass of the electroactive material in the electrode (g). The C_g of Co_3O_4@LDH NWs at 2 A g^{-1} is measured to be 818.6 C g^{-1} (C_a: 3.2 C cm^{-2}), which is much larger than those of Co_3O_4 NWAs (C_g: 514.7 C g^{-1}, C_a: 1.39 C cm^{-2}) and LDH NSs (C_g: 436.1 C g^{-1}, C_a: 0.39

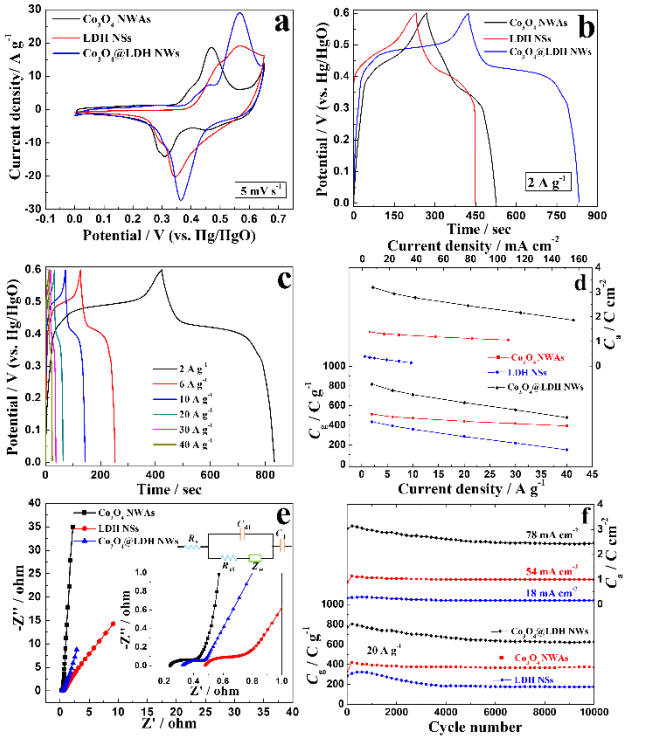

Fig. 5 (a) CV curves of Co_3O_4 NWAs, LDH NSs and Co_3O_4@LDH NWs electrodes at 5 mV s^{-1}. (b) GCD curves of Co_3O_4 NWAs, LDH NSs and Co_3O_4@LDH NWs electrodes at 2 A g^{-1}. (c) GCD curves of Co_3O_4@LDH NWs electrode at different current densities. (d) Current density dependence of the areal and gravimetric capacity of Co_3O_4 NWAs, LDH NSs and Co_3O_4@LDH NWs electrodes. (e) Nyquist plots of Co_3O_4 NWAs, LDH NSs and Co_3O_4@LDH NWs electrodes (inset: electrical equivalent circuit used for fitting impedance spectra). (f) Cycle stability of Co_3O_4 NWAs, LDH NSs and Co_3O_4@LDH NWs electrodes.

C cm^{-2}), revealing the advantage of 3D core-shell network structure for capacity improvement. The GCD curves of Co_3O_4@LDH NWs electrode measured at various current densities (2 to 40 A g^{-1}) in Fig. 5c possess good symmetry, verifying excellent electrochemical reversibility and charge-discharge properties. The changes of specific capacity along with the current density are illustrated in Fig. 5d. Within the entire current density (2 ~ 40 A g^{-1}), the 3D core-shell NWs delivers a greater C_g than Co_3O_4 NWAs and LDH NSs (the lower part in Fig. 5d). Note that even at the highest current density of 40 A g^{-1}, the C_g value of Co_3O_4@LDH NWs (479.3 C g^{-1}) remains at 58.6% of that measured at 2 A g^{-1}, thereby

exhibiting good rate capability. The C_a of all active materials versus current density plots are also shown in the upper part of Fig. 5d. In general, hetero-structured Co_3O_4@LDH NWs still demonstrate apparently superior C_a compared to the Co_3O_4 NWAs and LDH NSs. At the lowest current density of 7.8 mA cm^{-2}, a capacity of 3.2 C cm^{-2} can be achieved. While at the highest current density (156 mA cm^{-2}), the C_a of the network is maintained at 1.87 C cm^{-2}, which is still much larger than those of Co_3O_4 NWAs (1.39 C cm^{-2} at the lowest current density of 5.4 mA cm^{-2}) and LDH NSs (0.39 C cm^{-2} at the lowest current density of 1.8 mA cm^{-2}). The above features further demonstrate that the rational incorporation of active materials into well-defined core-shell hetero-structures can bring a strong synergetic effect on the final capacitive properties. Furthermore, the calculated capacity values in our work are higher than those previously reported 3D hierarchical core-shell electrodes, such as α-MnO_2 nanowires@δ-MnO_2 nanosheets (153.8 F g^{-1} at 20 A g^{-1}),[29] Fe_3O_4@C@NiAl-LDH (767.6 F g^{-1} at 1 A g^{-1}),[30] Co_3O_4@MnO_2 (0.56 F cm^{-2} at 11.25 mA cm^{-2}),[31] ZnO@MnO_2 (138.7 mF cm^{-2} at 1 mA cm^{-2}),[32] CuO@CoFe-LDH (0.86 F cm^{-2} at 2.5 mA cm^{-2})[33] and PEDOT@MnO_2 nanoparticles (~62 mF cm^{-2} at 5 mA cm^{-2}).[34]

To gain insight into detailed characteristics of the electrodes, the impedance of the Co_3O_4 NWAs, LDH NSs and Co_3O_4@LDH NWs electrodes were measured and simulated with an equivalent circuit, as shown in Fig. 5e. All curves include a semicircle intersecting the real axis in the high frequency region and an inclined line in the low-frequency region. The corresponding equivalent circuit is also presented in the upper-right position of Fig. 5e, where R_s is the internal resistance, R_{ct} is the Faradaic charge transfer resistance, C_{dl} is the double-layer capacitance, W is the Warburg diffusion element, and C_F is the limit capacitance.[27] In the high-frequency region, the intercept of the curve at the real axis (Z') is equal to R_s, which includes the resistance of the electrolyte, ohmic resistance of the active materials, and contact resistance at the active material/NF interface. In addition, the semicircle diameter at medium frequencies reflects R_{ct}, while the slope of straight line indicates the ion diffusion resistance. The smallest R_s (0.24 Ω) and largest slope of Co_3O_4 NWAs demonstrate that this 1D Co_3O_4 NWAs could be a good candidate of "core" materials. As expected, after growth of NiAl-LDH "shell" on Co_3O_4 NWAs "core", Co_3O_4@LDH NWs exhibit smaller R_s (0.33 Ω) and larger slope than bare LDH NSs (0.48 Ω), indicating the improved electrical conductivity and ion diffusion rate at the electrode/electrolyte interface. Moreover, the R_{ct} of Co_3O_4@LDH NWs electrode is the smallest (0.25 Ω), which reflects the highest accessible electroactive surface area.[27] In this regard, the pores and voids induced by the interconnected Co_3O_4@LDH NWs (Fig. 2e and 2f) facilitate the effective exposure of active surface sites for Faradaic reactions.

The long-term cycle stability of the electrodes was also tested for 10000 charge-discharge cycles at a current density of 20 A g^{-1}, as shown in Fig. 5f. For all electrodes, an increase in specific capacity during the initial cycles could result from the activation process of electroactive materials (Co_3O_4 or NiAl-LDH).[9, 24] Thereafter, all electrodes suffer from a loss of specific capacity during the subsequent cycles. For the Co_3O_4 NWAs electrode, a C_g value of 372 C g^{-1} (C_a: 1 C cm^{-2}) is maintained after 10000 cycles (increases by 13% of its initial capacity) at 20 A g^{-1} (54 mA cm^{-2}), confirming its suitability as a scaffold for the construction of core-shell nanostructures. However, the bare LDH NSs electrode shows poor stability and performance. Its specific capacity decreases from the initial value of 282 C g^{-1} (C_a: 0.25 C cm^{-2}) to 175.9 C g^{-1} (C_a: 0.16 C cm^{-2}) after the 10000-cycle test at 20 A g^{-1} (18 mA cm^{-2}). In the case of hetero-structured Co_3O_4@LDH NWs core-shell material, as the figure reveals, the electrode only undergoes a gradually declining with a retention rate of 83.3% during the first 5000 cycles and then the specific capacity keeps at about 645 C g^{-1} (C_a: 2.52 C cm^{-2}) in the subsequent 5000-cycle test. Intriguingly, this final specific capacity value is still superior to those of the pure Co_3O_4 NWAs (329 C g^{-1}) and LDH NSs (282 C g^{-1}) calculated at the 1st cycle. It can be observed that the Co_3O_4 NWAs exhibit small bending deformation (**Fig. 6**a) compared to the initial morphology (Fig. 2c and 2d). The nanowires tend to cluster at their tips to form sheaf-like structure, which may be due to the strong interaction forces between the long and thin nanowires.[24] However, the material preserves its nanowire arrays structure after cycling tests, maintaining the pathway for electrons and ions. For the LDH NSs electrode (Fig. 6b), some agglomerates can be found and the lip of the arrays is destroyed to a certain extent. Therefore, a drastic reduction of the C_g value and poor cyclic stability are observed. In Fig. 6c, the Co_3O_4@LDH NWs material could maintain the original 3D hierarchical core-shell structure except that the interconnected nanosheets "shell" become much sparser. As a result, the Co_3O_4@LDH NWs electrode exhibits better cycle stability than LDH NSs. Specifically, no cluster based sheaf-like structure can be observed in Co_3O_4@LDH NWs electrode after cycling test when compared with Co_3O_4 NWAs electrode due to the existence of interconnected NiAl-LDH shells. The results imply that the combination of Co_3O_4 and LDH with a unique network morphology and independent electroactivities into a single engineered hierarchical architecture can substantially enhance the electrochemical properties. This is quite different from the capacitance enhancement by previous core/shell nanostructure arrays, such as NiMn-LDH/CNT,[15] in which only the shell material was active material while the core material served as the nanowire current collector. It is expected that the synergistic contribution from 1D porous Co_3O_4 NWAs core, thin NiAl-LDH nanosheets shell, and the ordered hetero-structured network configuration should account for the excellent electrochemical performance (Fig. 6d). First, by growing directly from the 1D Co_3O_4 NWAs scaffold, the surfaces of NiAl-LDH nanosheets are well separated, making them fully available to contact with electrolyte, thus enhancing the specific capacity and cycling stability. Second, more pores and voids can be induced by the hierarchical Co_3O_4@LDH NWs (Fig. 2e and 2f), which are beneficial to the electrolyte infiltration, allowing the fast ion diffusion to obtain high rate performance.

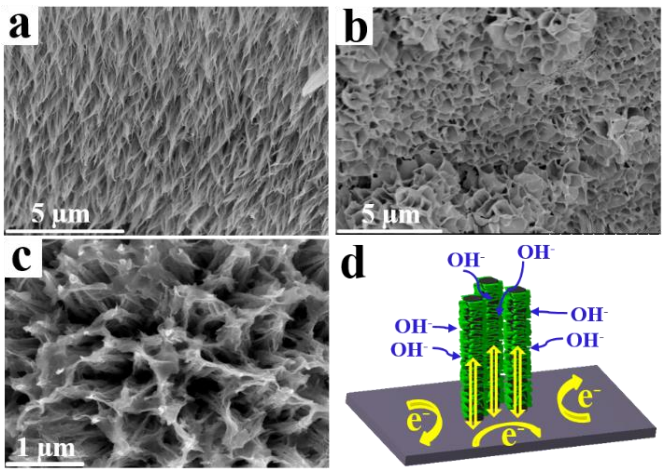

Fig. 6 SEM images of Co_3O_4 NWAs (a), LDH NSs (b) and Co_3O_4@LDH NWs (c) electrodes after cycling test at 20 A g^{-1}. (d) Schematic of the charge storage advantage of the hybrid nanoarrays.

It is noteworthy that the porous structure of Co_3O_4 NWAs would further increase the electrolyte-material contact area and enhance ion diffusion, which is very critical to high-power energy storage. Furthermore, the directly grown arrays can ensure good mechanical adhesion and electrical connection to the current collector (NF), avoiding the use of polymer binders and conducting additives which generally add extra contact resistance or weight.

To further investigate the practical application of this core-shell material, a hybrid supercapacitor (HSC) was prepared using Co_3O_4@LDH NWs as the positive electrode and GNS as the negative electrode (denoted as Co_3O_4@LDH//GNS). GNS was prepared according to our previous work.[35] In this study, to balance the charge storage in the positive and negative electrodes, the mass loading of Co_3O_4@LDH and GNS was 3.9 mg and 15.7 mg, respectively. According to electrochemical results of the positive and negative electrodes in a three-electrode system, it is expected that the fabricated HSC can afford a device with operation voltage of 1.6 V (inset of **Fig. 7**a). Fig. 7a presents the CV curves for the HSC device at various scan rates between 0 and 1.6 V. The CV curves deviate from a rectangular shape because of the Faradaic charge storage mechanism of Co_3O_4 and NiAl-LDH. Fig. 7b shows the GCD curves, from which the discharge part is almost symmetrical with its with its corresponding charge counterpart, demonstrating excellent electrochemical reversibility and good Coulombic efficiency. In Fig. 7c, the areal capacity values are

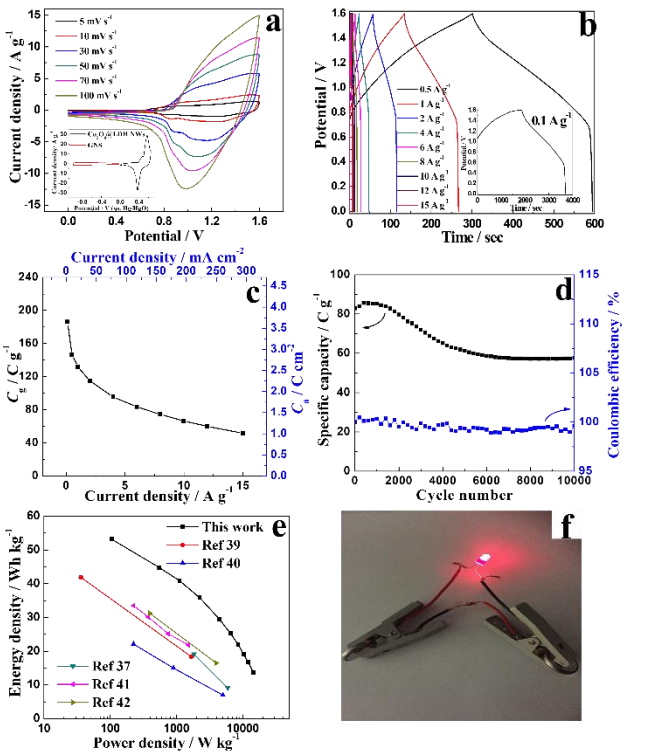

Fig. 7 (a) CV curves of Co_3O_4@LDH//GNS HSC device at different scan rates (inset: CV curves of Co_3O_4@LDH NWs and GNS at 5 mV s^{-1}). (b) GCD curves and (c) specific capacity of HSC device at different current densities. (d) Cycling performance of HSC device at 6 A g^{-1} for 10000 cycles. (e) Ragone plot of energy and power density of HSC device at various charge-discharge rates. (f) Digital photograph of HSC devices and lighted up LED.

calculated to be 3.65, 2.59, 1.64, 1.3 and 1.01 C cm^{-2} (C_g: 186.2, 132, 83.5, 66.4 and 51.6 C g^{-1}) at current densities of 1.96, 19.6, 117.6, 196 and 294 mA cm^{-2} (0.1, 1, 6, 10 and 15 A g^{-1}), respectively (based on the total mass of active materials in the positive and negative electrodes). The cycling durability of the HSC device is further evaluated at a current density of 6 A g^{-1} for 10000 cycles (Fig. 7d). The specific capacity gradually declines during the first 6000 cycles (about 71% retention) and then remains unchanged in the subsequent 4000-cycle test, which is comparable to reported HSCs in the literature such as $Ni(OH)_2$-MnO_2//RGO (76% after 3000 cycles),[36] $NiCo_2O_4$//AC (78% after 6000 cycles)[37] and PPy@MoO_3//AC (83% after 600 cycles).[38]

To evaluate practical performance of our device, the energy density and power density have been calculated from the following equations:

$E = 1/3.6 \cdot (I \int Vdt)/M$ ... (12)

$P = 3600E/t$ ... (13)

where E is the energy density (Wh kg^{-1}), I is the current (A), M is the total active mass of both electrodes (g), $\int Vdt$ is the galvanostatic discharge current area (V·s), P is the power density (W kg^{-1}) and t is the discharge time (s). The Ragone plot describing the relationship between energy and power density of the Co_3O_4@LDH//GNS HSC is shown in Fig. 7e. The device displays a high energy density of 53.2 Wh kg^{-1} at a power density of 105 W kg^{-1}. Even at a high power density of 16.4 kW kg^{-1}, the device still possesses an energy density of 11.2 Wh kg^{-1}. The results show that the HSC device achieved higher energy

density than the reported devices such as $NiCo_2O_4/Ni(OH)_2$//RGO,[39] CuO@MnO_2//MEGO,[40] $NiCo_2O_4$@MnO_2//AC,[37] Co_3O_4//AC[41] and $NiCo_2O_4$@$Co_xNi_{1-x}(OH)_2$//CMK-3.[42] In addition, a red LED was lighted up by two tandem prepared HSCs (Fig. 7f), exemplifying the potential practical application of our HSC devices.

The results demonstrate the importance and great potential application of 3D hereto-structured Co_3O_4@LDH NWs in the development of high performance energy storage devices. The excellent supercapacitive property of the hierarchical Co_3O_4@LDH NWs electrode could be attributed to the following reasons: (1) the core-shell architecture is composed of mesoporous Co_3O_4 core and NiAl-LDH shell with synergistic effects; (2) 1D Co_3O_4 NWAs grown directly on NF improves conductivity, offering effective electron transport to NiAl-LDH shells; (3) NiAl-LDH nanosheets are strongly anchored on the Co_3O_4 NWAs to form the unique hierarchical core-shell structure with good stability and integrity; (4) the pores and voids present within the nanoarrays are favorable to electrolyte infiltration and the rapid diffusion of ions by providing low-resistance pathways through the electrode surface.

Conclusions

In summary, 3D hereto-structured Co_3O_4@LDH NWs core-shell electrode with outstanding electrochemical performance was grown directly on nickel foam, which could be attributed to the synergistic contribution from the two promising materials (Co_3O_4 and NiAl-LDH), together with the merits of 3D core-shell network architecture. Besides, a high performance HSC device was fabricated using our Co_3O_4@LDH NWs as the positive electrode and GNS as the negative electrode, which achieved high energy and power densities and good cycling stability. We expected that the work presented here not only suggests the possibility to engineer Co_3O_4 and LDH into promising electrode materials, but presents a new way to create hybrid electrode architectures for energy storage devices, wearable and portable electronics.

Conflicts of interest

There are no conflicts to declare.

Acknowledgements

This work was supported by the Research Grants Council of the HKSAR Government (15217917), the Postdoctoral Fellowships Scheme of The Hong Kong Polytechnic University (1-YW3C), the Innovation and Technology Commission of the HKSAR Government to the Hong Kong Branch of National Rail Transit Electrification and Automation Engineering Technology Research Center (1-BBYW), the Science and Technology Development Fund of the Macau SAR Government (FDCT-098/2015/A3), and the Start-up Research Grant from the Research & Development Office at the University of Macau (SRG2015-00057-FST).

Notes and references

1. M. F. El-Kady, V. Strong, S. Dubin and R. B. Kaner, *Science*, 2012, **335**, 1326-1330.
2. K. Tao, X. Han, Q. X. Ma and L. Han, *Dalton Trans.*, 2018, **47**, 3496-3502.
3. M. Cheng, H. S. Fan, Y. J. Song, Y. M. Cui and R. M. Wang, *Dalton Trans.*, 2017, **46**, 9201-9209.
4. R. Oraon, A. De Adhikari, S. K. Tiwari and G. C. Nayak, *Dalton Trans.*, 2016, **45**, 9113-9126.
5. D. Selvakumar, A. Alsalme, A. Alswieleh and R. Jayavel, *J Alloy Compd.*, 2017, **723**, 995-1000.
6. L. Zhang, X. Zhang, L. Shen, B. Gao, L. Hao, X. Lu, F. Zhang, B. Ding and C. Yuan, *J. Power Sources*, 2012, **199**, 395-401.
7. P. F. Liu, J. J. Zhou, G. C. Li, M. K. Wu, K. Tao, F. Y. Yi, W. N. Zhao and L. Han, *Dalton Trans.*, 2017, **46**, 7388-7391.
8. Y. H. Zhao, X. Y. He, R. R. Chen, Q. Liu, J. Y. Liu, J. Yu, J. Q. Li, H. S. Zhang, H. X. Dong, M. L. Zhang and J. Wang, *Chem. Eng. J.*, 2018, **352**, 29-38.
9. L. J. Zhang, J. Wang, J. J. Zhu, X. G. Zhang, K. S. Hui and K. N. Hui, *J. Mater. Chem. A*, 2013, **1**, 9046-9053.
10. S. Singh, N. M. Shinde, Q. X. Xia, C. V. V. M. Gopi, J. M. Yun, R. S. Mane and K. H. Kim, *Dalton Trans.*, 2017, **46**, 12876-12883.
11. X. Y. He, R. M. Li, J. Y. Liu, Q. Liu, R. R. Chen, D. L. Song and J. Wang, *Chem. Eng. J.*, 2018, **334**, 1573-1583.
12. L. J. Zhang, K. N. Hui, K. S. Hui, X. Chen, R. Chen and H. W. Lee, *Int. J. Hydrogen Energ.*, 2016, **41**, 9443-9453.
13. Y. Zhao, L. Hu, S. Zhao and L. Wu, *Adv. Funct. Mater.*, 2016, **26**, 4085-4093.
14. J. Wang, X. Zhang, Q. Wei, H. Lv, Y. Tian, Z. Tong, X. Liu, J. Hao, H. Qu, J. Zhao, Y. Li and L. Mai, *Nano Energy*, 2016, **19**, 222-233.
15. J. W. Zhao, J. Chen, S. M. Xu, M. F. Shao, Q. Zhang, F. Wei, J. Ma, M. Wei, D. G. Evans and X. Duan, *Adv. Funct. Mater.*, 2014, **24**, 2938-2946.
16. J. Xu, C. Ma, J. Cao and Z. Chen, *Dalton Trans*, 2017, **46**, 3276-3283.
17. X. Y. He, Q. Liu, J. Y. Liu, R. M. Li, H. S. Zhang, R. R. Chen and J. Wang, *Chem. Eng. J.*, 2017, **325**, 134-143.
18. T. Peng, S. L. Fang, C. Liu, X. Y. Hou, H. P. Yang, R. J. Luo, Q. H. Yu, Y. Lu, H. L. Yan and Y. S. Luo, *Dalton Trans.*, 2017, **46**, 7451-7456.
19. Y. H. Zhao, X. Y. He, R. R. Chen, Q. Liu, J. Y. Liu, D. L. Song, H. S. Zhang, H. X. Dong, R. M. Li, M. L. Zhang and J. Wang, *Appl. Surf. Sci.*, 2018, **453**, 73-82.
20. D. He, G. L. Liu, A. Q. Pang, Y. Jiang, H. Suo and C. Zhao, *Dalton Trans.*, 2017, **46**, 1857-1863.
21. Y. S. Yesi, I. Shown, A. Ganguly, T. T. Ngo, L. C. Chen and K. H. Chen, *Chemsuschem*, 2016, **9**, 370-378.
22. F. Zhang, C. Yuan, X. Lu, L. Zhang, Q. Che and X. Zhang, *J. Power Sources*, 2012, **203**, 250-256.
23. B. Liu, D. Z. Kong, J. Zhang, Y. Wang, T. P. Chen, C. W. Cheng and H. Y. Yang, *J. Mater. Chem. A*, 2016, **4**, 3287-3296.
24. F. Zhang, C. Z. Yuan, X. J. Lu, L. J. Zhang, Q. Che and X. G. Zhang, *J. Power Sources*, 2012, **203**, 250-256.

25. Z. Gao, L. Zhang, C. Ma, Q. Zhou, Y. Tang, Z. Tu, W. Yang, L. Cui and Y. Li, *Biosens. Bioelectron.*, 2016, **80**, 511-518.
26. D. Z. Kong, J. S. Luo, Y. L. Wang, W. N. Ren, T. Yu, Y. S. Luo, Y. P. Yang and C. W. Cheng, *Adv. Funct. Mater.*, 2014, **24**, 3815-3826.
27. L. Zhang, K. N. Hui, K. S. Hui and H. Lee, *J. Power Sources*, 2016, **318**, 76-85.
28. F. S. Chen, X. H. Liu, Z. Zhang, N. Zhang, A. Q. Pan, S. Q. Liang and R. Z. Ma, *Dalton Trans.*, 2016, **45**, 15155-15161.
29. Z. Ma, G. Shao, Y. Fan, G. Wang, J. Song and D. Shen, *ACS Appl. Mater. Inter.*, 2016, **8**, 9050-9058.
30. L. Li, R. M. Li, S. L. Gai, F. He and P. P. Yang, *J. Mater. Chem. A*, 2014, **2**, 8758-8765.
31. J. P. Liu, J. Jiang, C. W. Cheng, H. X. Li, J. X. Zhang, H. Gong and H. J. Fan, *Adv. Mater.*, 2011, **23**, 2076-2081.
32. P. Yang, X. Xiao, Y. Li, Y. Ding, P. Qiang, X. Tan, W. Mai, Z. Lin, W. Wu, T. Li, H. Jin, P. Liu, J. Zhou, C. P. Wong and Z. L. Wang, *ACS Nano*, 2013, **7**, 2617-2626.
33. Z. Li, M. Shao, L. Zhou, R. Zhang, C. Zhang, J. Han, M. Wei, D. G. Evans and X. Duan, *Nano Energy*, 2016, **20**, 294-304.
34. R. Liu, J. Duay and S. B. Lee, *Acs Nano*, 2010, **4**, 4299-4307.
35. L. Zhang, R. Chen, K. N. Hui, K. S. Hui and H. Lee, *Chem. Eng. J.*, 2017, **325**, 554-563.
36. H. Chen, L. F. Hu, Y. Yan, R. C. Che, M. Chen and L. M. Wu, *Adv. Energy Mater.*, 2013, **3**, 1636-1646.
37. S. Khalid, C. B. Cao, L. Wang and Y. Q. Zhu, *Sci. Rep.*, 2016, **6**, 22699-22711.
38. Y. Liu, B. H. Zhang, Y. Q. Yang, Z. Chang, Z. B. Wen and Y. P. Wu, *J. Mater. Chem. A*, 2013, **1**, 13582-13587.
39. X. S. Yin, C. H. Tang, L. Y. Zhang, Z. G. Yu and H. Gong, *Sci. Rep.*, 2016, **6**, 21566-21577.
40. M. Huang, Y. X. Zhang, F. Li, Z. C. Wang, Alamusi, N. Hu, Z. Y. Wen and Q. Liu, *Sci. Rep.*, 2014, **4**, 4518-4526.
41. X. Zhang, Y. Q. Zhao and C. L. Xu, *Nanoscale*, 2014, **6**, 3638-3646.
42. K. B. Xu, R. J. Zou, W. Y. Li, Q. Liu, X. J. Liu, L. An and J. Q. Hu, *J. Mater. Chem. A*, 2014, **2**, 10090-10097.